

Determination of Optimal Angles for Variable Nutation Proton Magnetic Spin-Lattice, T_1 , and Spin-Spin, T_2 , Relaxation Times Measurement

Sean C.L. Deoni,^{1,2} Terry M. Peters,^{1–3} and Brian K. Rutt^{1–3*}

T_1 and T_2 can be rapidly determined with a combination of multiangle spoiled gradient recalled echo (SPGR) and steady-state free precession (SSFP) imaging. Previously, we demonstrated a simple method for determining the set of SPGR and SSFP angles that provided greater T_1 and T_2 precision than a set of uniformly spaced angles. In this article a more rigorous approach for determining angles is described. Weighted least-squares is also introduced for T_1 and T_2 estimation and a novel weighting function described. This new approach, suited for imaging applications where large T_1 and T_2 ranges are anticipated, provides high and uniform precision over a wide range of T_1 and T_2 values. *Magn Reson Med* 51:194–199, 2004. © 2003 Wiley-Liss, Inc.

Key words: T_1 mapping; T_2 mapping; fast imaging; human imaging; optimal angles

We have previously shown (1) that T_1 and T_2 can be calculated from variable nutation spoiled gradient recalled echo (SPGR), termed DESPOT1, and fully refocused steady-state free precession (SSFP) images, DESPOT2. In DESPOT1, T_1 is determined from a set of two or more SPGR images acquired with constant repetition time (TR) and varied flip angle (α). The SPGR signal equation can be linearized (2), allowing for rapid T_1 calculation from the raw signal data. This T_1 data is then combined with one or more SSFP images also acquired with constant TR and varied α to calculate T_2 (DESPOT2). The SSFP signal equation (3) may also be linearized (1), permitting rapid T_2 calculation. With this combined approach T_1 and T_2 can be measured significantly faster than with traditional inversion recovery and spin-echo methods, less than 13 min are required for a $25 \times 25 \times 10$ cm volumetric pair of maps with 1 mm^3 isotropic resolution.

In the previous literature (4,5), T_1 has traditionally been calculated from a standard set of uniformly spaced angles (i.e., 10, 20, 30, 40, 50, 60, 70, 80, 90, and 100 degrees). Examining the placement of these angles along the SPGR

signal curve for a variety of TR/ T_1 values shows that these angles do not always sample the peak region of the curve, resulting in low T_1 measurement accuracy and precision. The influence of angle placement on estimate precision was examined briefly in Ref. 1 and revealed the importance of tuning the angles depending on TR/ T_1 and TR/ T_2 .

In this article we describe an angle determination method based on the least-squares solution for T_1 and T_2 from the respective signal equations. Further, we introduce the use of a weighted least-squares algorithm to solve for T_1 and T_2 and define a weighting function that acts to preferentially select high signal/noise ratio (SNR) sample points. Comparing SNR values of in vivo and simulated T_1 and T_2 maps shows that the weighted least-squares algorithm combined with angles determined with the proposed method provide high and consistent precision across large T_1 and T_2 ranges.

THEORY

In our previous investigation (1), we examined the placement of angles along the SPGR and SSFP signal curves for various TR/ T_1 and TR/ T_2 cases and found that by uniformly spacing the sample points along the linearized regression line, we could more thoroughly sample the high SNR region of the curves. Angles meeting this uniform spacing requirement were termed “tuned” angles. To calculate the tuned angles, the minimum and maximum angles are first determined as those that provide 65% of the Ernst angle signal and the remaining angles are uniformly spaced along the regression line between.

We also examined the precision of T_1 and T_2 estimates made using just two “ideal” angles. By calculating the T_1 and T_2 precision as each of the two angles were varied from 1° to 90° , we found that the ideal angles are those whose signal is 71% of the Ernst angle signal. Although both the tuned and ideal angles provide significant gains in estimate precision over the traditional angle set, calculation of these angles requires a priori knowledge of average TR/ T_1 and TR/ T_2 . Further, the ideal angles maximize precision across only a small T_1 and T_2 value range. For large value ranges it is beneficial to include additional angles. To calculate the optimum angle set, we first consider the least-squares solution to the SPGR and SSFP signal equations.

DESPOT1

Following a similar approach as presented by Shrager et al. (6), the uncertainty of the T_1 value (δT_1) calculated from n SPGR images is derived by considering the least-squares fit

¹Imaging Research Laboratories, Robarts Research Institute, London, Ontario, Canada.

²Department of Medical Biophysics, University of Western Ontario, London, Ontario, Canada.

³Department of Diagnostic Radiology and Nuclear Medicine, University of Western Ontario, London, Ontario, Canada.

Grant sponsor: Canadian Institutes for Health Research; Grant numbers: MT-11540; GR-14973; Grant sponsors: Canadian Foundation for Innovation; University of Western Ontario; General Electric Medical Systems (Milwaukee, WI).

*Correspondence to: Brian K. Rutt, Imaging Research Laboratories, Robarts Research Institute, P.O. Box 5015, 100 Perth Drive, London, Ontario N6A 5K8, Canada. E-mail: brutt@imaging.robarts.ca

Received 14 April 2003; revised 22 August 2003; accepted 29 August 2003. DOI 10.1002/mrm.10661

Published online in Wiley InterScience (www.interscience.wiley.com).

of the experimental data, $S(i)$, with the theoretical signal equation (2):

$$f(\hat{M}_o, \hat{T}_1) = \sum_{i=1}^n \left[\frac{\hat{M}_o(1 - \hat{E}_1)\sin \alpha_i}{1 - \hat{E}_1 \cos \alpha_i} - S(i) \right]^2. \quad [1]$$

\hat{M}_o and \hat{E}_1 are the estimated values of the equilibrium longitudinal magnetization, M_o , and E_1 , where $E_1 = \exp(-TR/T_1)$. $S(i)$ can be denoted by:

$$S(i) = \frac{M_o(1 - E_1)\sin \alpha}{1 - E_1 \cos \alpha} + N(i). \quad [2]$$

$N(i)$ is a random noise function defined as $\langle N(i)N(j) \rangle = \sigma^2$ when $i = j$ and $\langle N(i)N(j) \rangle = 0$ when $i \neq j$.

As demonstrated in Appendix A, we find the expression for the variance in the T_1 estimate as:

$$\delta T_1^2 = \frac{T_1^4 \sigma^2}{M_o^2 TR^2} \left(\frac{a}{ac - b^2} \right) \quad [3]$$

where a , b , and c are as defined in the appendix and are functions of the sampled angles. Allowing $T_1/\delta T_1 = T_1 NR$ (T_1 -to-noise ratio, analogous to SNR), $M_o/\sigma = SNR_o$ and introducing a noise gain term, $G_1 = TR/T_1 \sqrt{(ac - b^2)/a}$, we rewrite Eq. [3] as:

$$T_1 NR = SNR_o \times G_1. \quad [4]$$

Here, SNR_o represents the maximum SNR and corresponds to the SNR of an image acquired with $\alpha = 90^\circ$ and $TR \gg T_1$. Finally, we relate the SNR of the T_1 map made from n images to the SNR of n averaged SPGR images acquired at the Ernst angle, SNR_E , as:

$$T_1 NR = \sqrt{n} SNR_E \times H_1 \quad [5]$$

where $H_1 = (\sqrt{2TR/T_1})/(\sqrt{n} TR/T_1) \times G_1$.

DESPOT2

Following a similar methodology as above, we derive, in Appendix B, the equation for variance in the T_2 estimate calculated from n SSFP images as:

$$\delta T_2^2 = \frac{\sigma^2 T_2^4}{M_o^2 TR^2} \left(\frac{x}{xz - y^2} \right) \quad [6]$$

where x , y , and z are defined in the appendix and are functions of the sampled angles. We rewrite Eq. [6] in terms of the T_2 -to-noise ratio, $T_2 NR$, and SNR_o as:

$$T_2 NR = SNR_o \times G_2 \quad [7]$$

where $G_2 = TR/T_2 \sqrt{(xz - y^2)/x}$. Once again, SNR_o is defined as the SNR of an image collected with $\alpha = 90^\circ$ and $TR \gg T_1$ and T_2 . As before, we relate this SNR to the SNR of n averaged SSFP images acquired at the Ernst angle as:

$$T_2 NR = \sqrt{n} SNR_E \times H_2 \quad [8a]$$

where:

$$H_2 = \frac{1 - E_1 E_2 - (E_1 - E_2) \times E_1 - E_2/1 - E_1 E_2}{\sqrt{n} (1 - E_1) \times \sqrt{1 - (E_1 - E_2/1 - E_1 E_2)^2}} \times G_2. \quad [8b]$$

Weighted Least-Squares Analysis

By placing greater influence on high SNR points, additional gains in T_1 and T_2 precision may be achieved. Therefore, we introduce a weighted least-squares algorithm with the weighting function, $W_i = S\alpha_i/S\alpha_E$, where $S\alpha_i$ is the signal acquired at flip angle α_i and $S\alpha_E$ is the signal acquired at the Ernst angle. W_i is easily included into the T_1 and T_2 variance equations (Eqs. [3] and [6]) with a redefinition of a , b , c , x , y , and z as: $a' = \sum_{i=1}^n W_i X_i^2$, $b' = \sum_{i=1}^n W_i X_i Z_i$, $c' = \sum_{i=1}^n W_i Z_i^2$, $x' = \sum_{i=1}^n W_i A_i^2$, $y' = \sum_{i=1}^n W_i A_i C_i$ and $z' = \sum_{i=1}^n W_i C_i^2$.

The optimum set of angles can now be determined by calculating the angles that maximize Eqs. [5] and [8].

MATERIALS AND METHODS

Determination of Angles

To determine the set of flip angles maximizing Eqs. [5] and [8] with and without W_i included, we used a genetic algorithm (GA) optimization approach (7). The advantage of GA is that a model describing the angle spacing (i.e., linearly spaced, logarithmically spaced, etc.) is not required.

To calculate the optimum angles, we begin with a population of 250 sets of angles, each representing a possible solution. The fitness ($T_1 NR$ or $T_2 NR$) is calculated for each of these sets (parents) and pairs of parents are chosen using roulette-wheel selection (7) to create new "child" solutions by averaging the parents, e.g., parent A = {1, 5, 10} and parent B = {2, 9, 15} yield child A = {1.5, 7, 12.5}. To add diversity, one angle in 5% of the children is randomly changed. The child solutions replace the parents and the process is repeated for 5000 iterations. The fittest individual at the end of the 5000 iterations is considered the optimum set of angles. Specific algorithm parameters used were: TR = 5 ms, T_1 and T_2 were the average of white matter and cerebral spinal fluid ((600+4500)/2 = 2550 ms for T_1 and (65+800)/2 = 430 ms for T_2 (8,9)). Angles were constrained to be integers within the ranges of 1–60° and 1–90° for DESPOT1 and DESPOT2, respectively. The algorithm was repeated 50 times to determine its reproducibility.

Simulation Methods

$T_1 NR$ and $T_2 NR$ of the tuned, ideal, GA, and weighted GA angle sets were evaluated using Eqs. [5] and [8] over a range of T_1 (50–5000 ms) and T_2 (10–500 ms) values. The ideal and tuned angles were calculated using the average T_1 and T_2 values cited above. For the ideal angles, data at

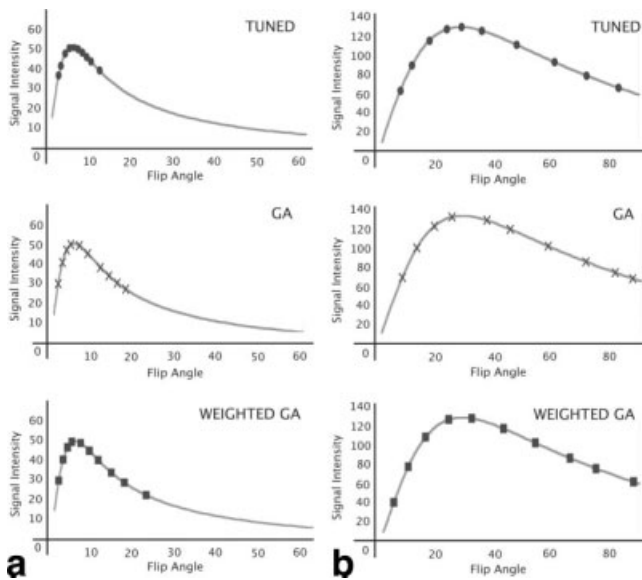


FIG. 1. Placement of the three sets of DESPOT1 and DESPOT2 angles along the (a) SPGR and (b) SSFP signal curves. The curves correspond to average brain T_1 and T_2 values. Tuned angles are shown with circles, GA angles with crosses, and weighted GA angles with squares.

each angle was “acquired” five times to keep the exam time constant. For T_1 , the flip angles were: tuned = $\{2^\circ, 3^\circ, 4^\circ, 5^\circ, 6^\circ, 7^\circ, 8^\circ, 9^\circ, 10^\circ, 12^\circ\}$, ideal = $\{3^\circ, 12^\circ\}$, GA = $\{2^\circ, 3^\circ, 4^\circ, 5^\circ, 7^\circ, 9^\circ, 12^\circ, 14^\circ, 16^\circ, 18^\circ\}$ and weighted GA = $\{2^\circ, 3^\circ, 4^\circ, 5^\circ, 7^\circ, 9^\circ, 11^\circ, 14^\circ, 17^\circ, 22^\circ\}$. T_2 flip angles were: tuned = $\{8^\circ, 12^\circ, 18^\circ, 24^\circ, 29^\circ, 36^\circ, 48^\circ, 61^\circ, 72^\circ, 83^\circ\}$, ideal = $\{20^\circ, 80^\circ\}$, GA = $\{8^\circ, 13^\circ, 19^\circ, 25^\circ, 37^\circ, 45^\circ, 58^\circ, 71^\circ, 81^\circ, 87^\circ\}$, and weighted GA = $\{5^\circ, 10^\circ, 16^\circ, 24^\circ, 32^\circ, 43^\circ, 54^\circ, 66^\circ, 75^\circ, 88^\circ\}$.

Experimental Methods

3D axial brain images were acquired from a volunteer at the level of the lateral ventricles. Informed consent was obtained and the study was performed with approval from the Ethics Review Board Committee at the University of Western Ontario. All images were acquired on a clinical 1.5 T CV/i system (GE Medical Systems, Milwaukee, WI). T_1NR and T_2NR values of six brain regions: frontal white matter (WM), frontal gray matter (GM), cerebral spinal fluid (CSF), thalamus (Thal), globus pallidus (GP), and putamen (Put) were calculated from each angle set and compared. Mean and standard error of the mean values were calculated from four regions of interest within each tissue. Data was also collected from a water-filled ball phantom.

T_1 values were calculated from data collected with a $128 \times 128 \times 50$ matrix with $25 \text{ cm}^2 \times 10 \text{ cm}$ field of view (FOV), TR = 3.4 ms, and TE = 1.1 ms. Total imaging time in each case was held constant at 3.75 min. T_2 was calculated from data acquired with TR = 3.8 ms and TE = 1.9 ms. Total imaging time in each case was 4 min. By keeping the TR of the SSFP acquisition less than 5 ms, the well-known banding artifact (10,11) due to resonant offset

was avoided. Flip angles used for T_1 and T_2 acquisitions were the same as in the simulation.

In the weighted least-squares algorithm, the Ernst angle was first calculated from the weighted GA angle data using nonweighted least-squares. The weights for each sample point were then determined and the T_1 or T_2 recalculated using weighted least-squares.

RESULTS

Determination of Angles

Using our GA optimization approach, the following sets of angles were determined: T_1 : $\{2^\circ, 3^\circ, 4^\circ, 5^\circ, 7^\circ, 9^\circ, 12^\circ, 14^\circ, 16^\circ, 18^\circ\}$ without weighting and $\{2^\circ, 3^\circ, 4^\circ, 5^\circ, 7^\circ, 9^\circ, 11^\circ, 14^\circ, 17^\circ, 22^\circ\}$ with weighting. For T_2 : $\{8^\circ, 13^\circ, 19^\circ, 25^\circ, 37^\circ, 45^\circ, 58^\circ, 71^\circ, 81^\circ, 87^\circ\}$ without weighting and $\{5^\circ, 10^\circ, 16^\circ, 24^\circ, 32^\circ, 43^\circ, 54^\circ, 66^\circ, 75^\circ, 88^\circ\}$ with weighting. From the 50 trials, the average reproducibility was 0.76% and 1.3% for T_1 and T_2 , respectively.

Examining the placement of these angles along the signal curve (Fig. 1), we notice a spreading of the angles as we move from the tuned to GA to weighted GA angles. This spreading results in an increased dynamic range (DR) of the regression line. As stated in Ref. 1, precision is dependent on both DR and SNR. The large DR provided by the GA-determined angles does not result in loss of average SNR because the majority of points are located near the peak, with few points separated along the tails of the curve. The DR of the tuned angles may be increased by

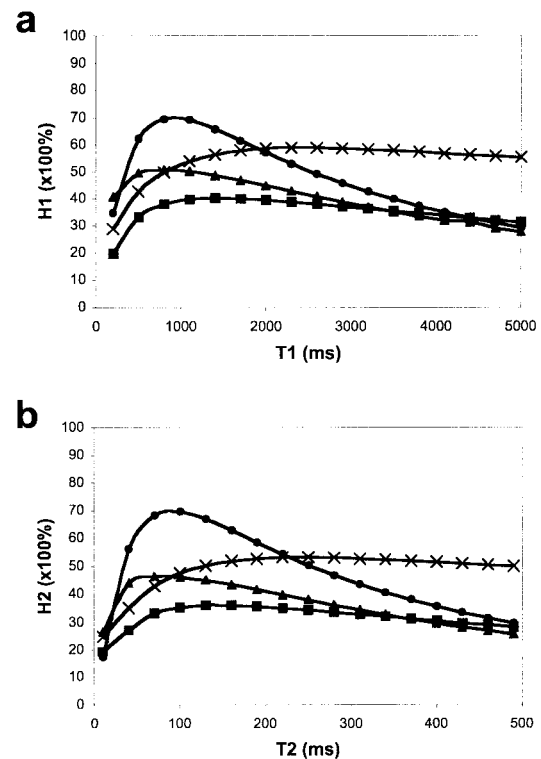


FIG. 2. Theoretical (a) $H_1 \times 100\%$ and (b) $H_2 \times 100\%$ values evaluated across a range of T_1 and T_2 values for the different angle sets. Square = tuned, circle = ideal, triangle = GA, cross = weighted GA.

adjusting the minimum and maximum angles so that, for example, they correspond to 50% of the Ernst signal. However, this lowers the average SNR of the points and, therefore, decreases H_1 , H_2 , and the precision of the estimates.

Simulation Results

$H_1 \times 100\%$ and $H_2 \times 100\%$ values evaluated over a range of T_1 and T_2 values are shown in Fig. 2. Although peak precision is obtained through the use of the averaged ideal angles for $T_1 < 2000$ ms and $T_2 < 230$ ms, the multiple angle calculations show a more uniform precision profile across the T_1 and T_2 range. This precision consistency is important in cases where T_1 and T_2 are not known (and the ideal angles cannot be calculated) or when a large range of T_1 or T_2 values is anticipated. Comparing the multiangle results, we notice that the GA angles offer an increase in precision of 35% over the tuned angles. The advantage of the weighted least-squares algorithm is clearly shown, with a precision increase of 28% over the nonweighted GA angles and 80% over the tuned angles.

Figure 2 also reveals the efficiency (defined as the SNR of the T_1 or T_2 map divided by the SNR of an image acquired repeatedly at the Ernst angle and averaged) of DESPOT1 and DESPOT2. With ideal angles, the method offers 70% peak efficiency. Using more than two angles decreases the efficiency slightly with 10 weighted angles affording 60% peak efficiency.

Experimental Data

Relative brain T_1NR and T_2NR values for six tissues and water, calculated from each angle set, are shown in Fig. 3. Over the relatively narrow range of T_1 and T_2 's in the brain, maximum precision is obtained when the ideal angles are used, with CSF being the lone exception. The precision of CSF and water are maximal with the weighted GA angles. From Fig. 2 we see that the multiple angles will not begin to outperform the ideal angles until $T_1 > 2000$ ms and $T_2 > 230$ ms, so these results are not surprising. Comparison of the multiangle results reveals similar trends as seen in the simulation results. In general, the penalty of using multiple flip angles on the SNR is modest and does not significantly limit the use of the method in applications where large T_1 and T_2 ranges are expected.

Average T_1 and T_2 values calculated were as follows (in ms): WM (621, 63), GM (1283, 105), CSF (4403, 780), GP (780, 68), Thal (903, 91), Put (984, 79), and water (3163, 2372). These results were calculated using the weighted GA angle data and are representative of the average values calculated with the other angle sets.

DISCUSSION

The results presented herein demonstrate the influence of angle choice on T_1 and T_2 precision and highlight the complexity of determining the optimal angles for DESPOT1 and DESPOT2. The TR/T_1 and TR/T_2 terms in Eqs. [5] and [8] indicate that no single set of angles will maximize the precision for all T_1 and T_2 values, rather, the precision will be maximal only for a target T_1 and T_2 range. In general, as the number of flip angles is increased, the

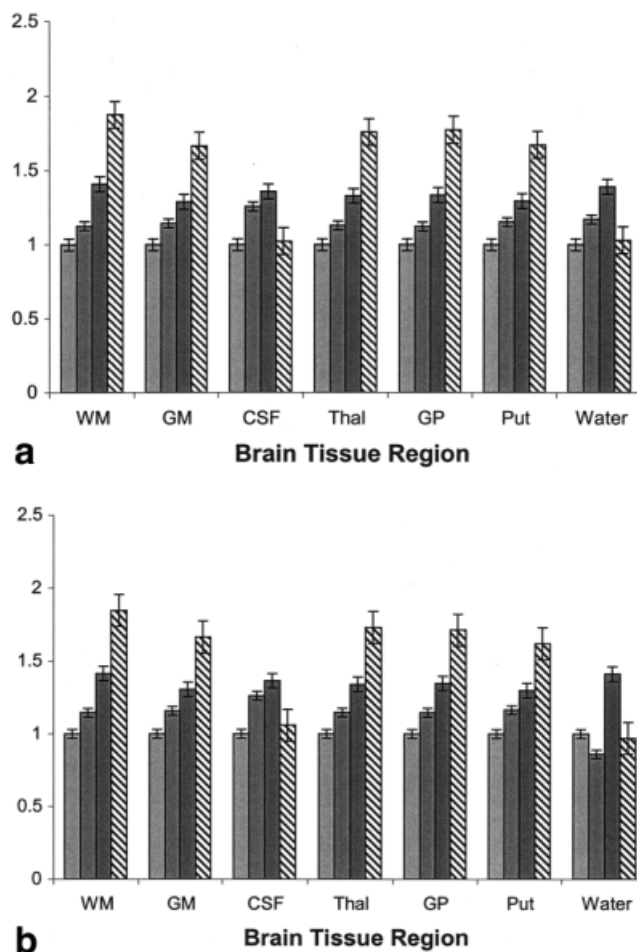


FIG. 3. Relative (a) T_1NR and (b) T_2NR values for six common brain tissues and distilled water calculated from DESPOT1 and DESPOT2 data acquired with 10 tuned angles, 10 GA angles (with and without weighting), and the two ideal angles averaged five times each. Error bars represent the standard error of the mean.

maximal precision decreases while the precision profile becomes more uniform. It is clear, then, that if maximum precision is desired over a small T_1 and T_2 range, data should be acquired at just the two ideal flip angles. However, when T_1 and T_2 are not known, or when uniform precision is desired over a large range of values, such as in in vivo abdominal and pelvic imaging or in vitro sample imaging, more than two flip angles should be sampled. The proposed angle determination method has been developed specifically for these applications to provide more uniform precision compared with the tuned angle approach. Although the computation time for the GA approach is ~ 30 sec, compared to less than 1 sec required to calculate the ideal angles, we do not feel this represents a significant limitation.

The utility of a weighted least-squares algorithm to calculate T_1 and T_2 has also been demonstrated in the results. By maximizing the influence of high SNR sample points in each calculation the algorithm further helps to create a uniform precision profile in addition to increasing the average precision of the multiangle estimates. Although the weighted algorithm increases the required computa-

tion time, the higher precision of the results justifies this increase.

A final point illustrated in the results is the maximal efficiency of the DESPOT1 and DESPOT2 T_1 and T_2 measurement methods. From Fig. 2 we see that when the ideal angles are used, the efficiencies of the methods are $\sim 70\%$. Since the ideal angles are defined as those that provide 71% of the Ernst angle signal, the mapping process results in only slight SNR degradation compared with simply averaging the two images together. As expected, the inclusion of addition angles reduces the SNR of the maps, but only by 14% compared to the ideal angle case. Therefore, we feel that the penalty of using multiple flip angles on SNR is modest and does not significantly limit the use of the method in applications where large T_1 and T_2 ranges are expected.

CONCLUSION

We have presented an angle determination method and weighted least-squares algorithm for DESPOT1 and DESPOT2 providing high and consistent T_1 and T_2 estimate precision. The method is easy to implement, requires little computation time, and affords high and uniform precision across large T_1 and T_2 ranges. The method is therefore particularly suited to imaging applications where such ranges are anticipated.

ACKNOWLEDGMENTS

We thank Glencora Borradaile for her insight into the world of GA. B.K.R. receives salary support from the Barnett-Ivey Heart and Stroke Foundation of Ontario Endowed Chair award.

APPENDIX A

To determine expressions for \hat{M}_o and \hat{T}_1 , calculate the derivatives of Eq. [1] with respect to \hat{M}_o and \hat{T}_1 and setting both to zeros yields:

$$\frac{\partial f}{\partial \hat{M}_o} = 2 \sum_{i=1}^n \left[\frac{\hat{M}_o(1 - \hat{E}_1)\sin \alpha_i}{1 - \hat{E}_1 \cos \alpha_i} - S(i) \right] \times \hat{X}_i = 0 \quad [\text{A1a}]$$

and

$$\frac{\partial f}{\partial \hat{T}_1} = 2 \sum_{i=1}^n \left[\frac{M_o(1 - \hat{E}_1)\sin \alpha_i}{1 - \hat{E}_1 \cos \alpha_i} - S(i) \right] \times \hat{Y}_i = 0 \quad [\text{A1b}]$$

where

$$\hat{X}_i = \frac{(1 - \hat{E}_1)\sin \alpha_i}{1 - \hat{E}_1 \cos \alpha_i}, \quad [\text{A1c}]$$

$$\hat{Y}_i = \frac{M_o TR}{\hat{T}_1^2} \hat{Z}_i, \quad [\text{A1d}]$$

and

$$\hat{Z}_i = \frac{(1 - \hat{E}_1)\hat{E}_1 \sin \alpha_i \cos \alpha_i}{(1 - \hat{E}_1 \cos \alpha_i)^2} - \frac{\hat{E}_1 \sin \alpha_i}{1 - \hat{E}_1 \cos \alpha_i}. \quad [\text{A1e}]$$

Unfortunately, Eqs. [A1a] and [A1b] are coupled nonlinear equations that are difficult to solve explicitly. To obtain independent expressions for δM_o and δT_1 we define the following, $\hat{M}_o = M_o + \delta M_o$ and $\hat{T}_1 = T_1 + \delta T_1$ and expand the bracketed portions of Eqs. [A1a] and [A1b] using the simplified form of the 2D Taylor series approximation:

$$\frac{\partial f}{\partial \hat{M}_o} = \sum_{i=1}^n [\delta M_o \hat{X}_i + \delta T_1 \hat{Y}_i - N(i)] \times \hat{X}_i = 0 \quad [\text{A2a}]$$

and

$$\frac{\partial f}{\partial \hat{T}_1} = \sum_{i=1}^n [\delta M_o \hat{X}_i + \delta T_1 \hat{Y}_i - N(i)] \times \hat{Y}_i = 0. \quad [\text{A2b}]$$

Additionally, we assume that the SNR is sufficiently high, such that $X_i \approx \hat{X}_i$, $Y_i \approx \hat{Y}_i$, and $Z_i \approx \hat{Z}_i$, where,

$$X_i = \frac{(1 - E_1)\sin \alpha_i}{1 - E_1 \cos \alpha_i}, \quad Y_i = \frac{M_o TR}{T_1^2} Z_i$$

and

$$Z_i = \frac{(1 - E_1)E_1 \sin \alpha_i \cos \alpha_i}{(1 - E_1 \cos \alpha_i)^2} - \frac{E_1 \sin \alpha_i}{1 - E_1 \cos \alpha_i}.$$

Expanding Eq. [A2] with these simplifications gives:

$$\delta M_o \sum_{i=1}^n X_i^2 + \delta T_1 \sum_{i=1}^n X_i Y_i = \sum_{i=1}^n N(i) X_i \quad [\text{A3a}]$$

and

$$\delta M_o \sum_{i=1}^n X_i Y_i + \delta T_1 \sum_{i=1}^n Y_i^2 = \sum_{i=1}^n N(i) Y_i. \quad [\text{A3b}]$$

Here we are left with two equations and two unknowns. Solving first for δM_o from Eq. [A3] gives:

$$\delta M_o = \frac{\sum_{i=1}^n N(i) X_i - \delta T_1 \sum_{i=1}^n Y_i X_i}{\sum_{i=1}^n X_i^2}, \quad [\text{A4a}]$$

which we substitute into Eq. [A3b] and obtain an expression for δT_1 :

$$\delta T_1 = \frac{\sum_{i=1}^n N(i) Y_i \sum_{i=1}^n X_i^2 - \sum_{i=1}^n N(i) X_i \sum_{i=1}^n X_i Y_i}{\sum_{i=1}^n X_i^2 \sum_{i=1}^n Y_i^2 - \left(\sum_{i=1}^n X_i Y_i \right)^2}. \quad [\text{A4b}]$$

Here, we factor out the $M_0 TR/T_1^2$ term from Y_i , square both sides of the result and define $a = \sum_{i=1}^n X_i^2$, $b = \sum_{i=1}^n X_i Z_i$ and $c = \sum_{i=1}^n Z_i^2$ and obtain the result:

$$\delta T_1^2 = \frac{T_1^4 \sigma^2}{M_0^2 TR^2} \left(\frac{a}{ac - b^2} \right). \quad [\text{A5}]$$

APPENDIX B

Solving for δT_2 from the least-squares fit of the experimental data to the signal model:

$$f(\hat{M}_0, \hat{T}_2) = \sum_{i=1}^n \left[\frac{\hat{M}_0 (1 - E_1) \sin \alpha_i}{1 - E_1 \hat{E}_2 - (E_1 - \hat{E}_2) \cos \alpha_i} - S(i) \right]^2 \quad [\text{A6}]$$

we find:

$$\frac{\delta T_2^2}{T_2^2} = \frac{\sigma^2 T_2^2}{M_0^2 TR^2} \left(\frac{x}{xz - y^2} \right) \quad [\text{A7}]$$

where

$$x = \sum_{i=1}^n A_i^2, \quad y = \sum_{i=1}^n A_i C_i, \quad z = \sum_{i=1}^n C_i^2$$

and

$$\hat{A}_i = \frac{(1 - E_1) \sin \alpha_i}{1 - E_1 \hat{E}_2 - (E_1 - \hat{E}_2) \cos \alpha_i}, \quad \hat{B}_i = \frac{\hat{M}_0 TR}{\hat{T}_2^2} \hat{C}_i,$$

and

$$\hat{C}_i = \frac{(1 - E_1) \sin \alpha_i}{(1 - E_1 \hat{E}_2 - (E_1 - \hat{E}_2) \cos \alpha_i)^2} (-\hat{E}_2 \cos \alpha_i - E_1 \hat{E}_2).$$

REFERENCES

1. Deoni SCL, Rutt BK, Peters TM. Rapid combined T_1 and T_2 mapping using gradient acquisition in the steady state. *Magn Reson Med* 2003; 49:515–526.
2. Christensen KA, Grand DM, Schulman EM, Walling C. Optimal determination of relaxation times of Fourier transform nuclear magnetic resonance. Determination of spin-lattice relaxation times in chemically polarized species. *J Phys Chem* 1974;78:1971–1977.
3. Carr HY. Steady state free precession in nuclear magnetic resonance. *Phys Rev* 1958;112:1693–1701.
4. Homer J, Beevers MS. Driven-equilibrium single-pulse observation of T_1 relaxation. A re-evaluation of a rapid 'new' method for determining NMR spin-lattice relaxation times. *J Magn Reson* 1985;63:287–297.
5. Wang HZ, Riederer SJ, Lee JN. Optimizing the precision in T_1 relaxation estimation using limited flip angles. *Magn Reson Med* 1987;5: 399–416.
6. Shrager RI, Weiss GH, Spencer RG. Optimal time spacings for T_2 measurements: monoexponential and biexponential systems. *NMR Biomed* 1998;11:297–305.
7. Davis L. Handbook of genetic algorithms. New York: Van Nostrand; 1991.
8. Chen KH. In vivo tissue characterization of human brain by chisquares parameter maps: multiparameter proton T_2 -relaxation analysis. *Magn Reson Imag* 1994;12:1099–1109.
9. Breger RK, Rimm AA, Fischer ME, Papke RA, Haughton VM. T_1 and T_2 measurements on a 1.5T commercial MR imager. *Radiology* 1989;171: 273–276.
10. Zur Y, Stokar S, Bendel P. An analysis of fast imaging sequences with steady-state transverse magnetization refocusing. *Magn Reson Med* 1988;6:175–193.
11. Scheffler K, Hennig J. Is TrueFISP a gradient-echo or spin-echo sequence? *Magn Reson Med* 2003;49:395–397.